Journal of Alloys and Compounds 1022 (2025) 180039

Contents lists available at ScienceDirect

Journal of Alloys and Compounds

journal homepage: www.elsevier.com/locate/jalcom

Phase segregation in $K_xNa_{1-x}NbO_3$ films grown by large-scale confocal RF sputtering

Giulia Pavese [a], Federico Orlando [a,b], Silvia Picozzi [b,c], Edoardo Albisetti [a], Federico Maspero [a], Marco Asa [a], Fabio Melzi [d], Laura Castoldi [d], Riccardo Bertacco [a], Miguel Badillo [a,*]

[a] Dipartimento di Fisica, PoliFAB, Politecnico di Milano, Via Giuseppe Colombo 81, Milano 20133, Italy
[b] Consiglio Nazionale delle Ricerche CNR-SPIN, c/o Università degli Studi G. D'Annunzio, Chieti, Italy
[c] Dipartimento di Scienza dei Materiali, Università di Milano Bicocca, Via Roberto Cozzi 55, Milano 20125, Italy
[d] STMicroelectronics, APMS-R&D MEMS, Via Camillo Olivetti 2, Agrate Brianza, Monza Brianza 20864, Italy

ARTICLE INFO

Keywords:
Piezoelectricity
Ferroelectricity
Perovskites
$K_xNa_{1-x}NbO_3$
Thin films
Sputtering
Wafer-scale

ABSTRACT

As of now, KNN is the most viable alternative to PZT. Sputtering deposition is very suitable for large-scale production of thin films, but some challenges need to be overcome. We deposited KNN films on 8" wafers by using an EVATEC's Clusterline-200E sputtering machine. Lower growth pressure and high annealing temperatures promote larger deposition rates, higher crystallinity, and larger *c*-lattice parameters of the perovskite phase. KNN films thus obtained display a general {001} preferred orientation out of plane with evident appearance of the (001) polar direction. Therefore, ferroelectric response is observed in most films, with a maximum $2Pr = 21$ $\mu C/cm^2$ for films grown at low pressure and annealed at 700 °C under N_2+O_2 atmosphere. Depending on growth and annealing conditions, however, initially amorphous KNN films crystallize into segregated Na-rich polar perovskite and spurious pyrochlore phases. A Na-rich perovskite ferroelectric phase forms into "volcano-like" islands with composition $K_xNa_{1-x}NbO_3$, where $x = 0.2–0.3$. The stoichiometry aligns with other known non-equimolar KNN morphotropic phase boundaries and is supported by first-principles calculations. As K diffuses away from the islands and escapes from films at a higher rate than Na, the remaining part of the film forms a chemically unstable K-rich pyrochlore phase, of the type $K_4Nb_6O_{17}$, that easily degrades during lithographic patterning. We suggest that enhanced KNN films can be produced by RF sputtering not only by counteracting Na and K loss by using alkali-excess targets, but also by employing over-stoichiometric targets with compositions richer in Na (70–80 at%).

1. Introduction

In recent years, $K_xNa_{1-x}NbO_3$ (KNN) has been regarded as a promising replacement for PZT, the most widely used piezoelectric material whose applications span in several fields, such as aerospace, telecommunications and diagnostics [1,2]. Extensive research has been done for bulk KNN ceramics, achieving very good properties, like a high Curie temperature of 400 °C [3] and d_{33} coefficient of 416 pC/N, demonstrated by Saito et al. for KNN textured ceramics with (001) $NaNbO_3$ seed layers [4]. Record values of 570 pC/N have been reached by Wu et al. [5]. Despite its promise, KNN faces significant challenges that hinder its widespread application. Key issues include the high temperatures required to achieve the polar tetragonal or orthorhombic phases (500 °C - 700 °C) [6,7] and the high leakage caused by A-site and oxygen vacancies [8–11]. These factors can significantly reduce the operational voltage of devices and result in critical failure [12]. For KNN thin films, in addition to these problems, a major obstacle is the scale-up from small research samples to wafer-scale production. For industrial purposes, the material should be grown at possibly at low temperature, uniform at large scale and with a reasonably high growth rate [13]. Achieving those requirements, however, can have significant side effects on KNN films quality. For example, the literature reports the formation of unwanted pyrochlore secondary phases at low processing temperatures. Pyrochlore phases are non-polar and therefore they do not contribute to the piezoelectric performance of KNN. The presence of such phases has been studied extensively in PZT thin films [14–17]. In fewer numbers, similar studies also exist for KNN, for example, the work by Ahn et al. [10], Kim et al. [18] and Jacques et al. [19]. An aspect that has rarely been

* Corresponding author.
E-mail address: miguelangel.badillo@polimi.it (M. Badillo).

https://doi.org/10.1016/j.jallcom.2025.180039
Received 28 January 2025; Received in revised form 24 March 2025; Accepted 25 March 2025
Available online 27 March 2025

explored or reported in the literature is the diffusion of Na and K in KNN during processing and its influence on the formation of perovskite and pyrochlore phases in KNN films.

In this paper, we discuss the growth of KNN films on 8'' wafers with an industrial RF sputtering in Ar atmosphere from a stoichiometric $K_{0.5}Na_{0.5}NbO_3$ target. We show that, starting from amorphous films, annealing in a $N_2 + O_2$ atmosphere at high temperature promotes a partial crystallization of KNN films, resulting in (100/001) preferential orientation and in ferroelectric behavior, superimposed to leaky dielectric characteristic. We demonstrate that KNN films properties are, in general, dependent on the Ar flow during the growth and on the annealing temperature. On average, all the films are characterized by a deficiency of alkali ions, resulting in the ratio (K+Na)/Nb around 0.8. Potassium tends to evaporate at high annealing temperatures, while sodium follows an opposite trend. In particular, we observe the nucleation of a segregated Na-rich $K_xNa_{x-1}NbO_3$ perovskite phase ($0.2 \leq x \leq 0.3$) in the form of islands, together with an unwanted pyrochlore phase with a composition close to $A_4Nb_6O_{17}$, where A = K+Na and A/Nb = 0.67. The composition of the segregated perovskite phase $K_xNa_{1-x}NbO_3$ is close to the other two morphotropic phase boundaries with x = 0.17 and x = 0.35, that are seldom reported in literature [20–22], and matches our first-principles results favoring a concentration of x = 0.17. By C-AFM and local IV measurements, we demonstrate that the ferroelectric response of the films is given, as expected, by the perovskite segregated regions, while the pyrochlore displays a leaky dielectric behavior. Given a better retention of Na at high temperatures, and the natural evolution of the film towards a Na-rich perovskite, we predict that a Na-rich target may facilitate better control over the perovskite crystallization, preventing phase segregation and unwanted pyrochlore phases. Additionally, our analysis suggests the need to compensate for alkali loss by incorporating extra alkali into the targets and growing KNN films in an oxygen-rich atmosphere to further stabilize the perovskite phase.

2. Methods

Nominal $K_{0.5}Na_{0.5}NbO_3$ films were deposited on 8" wafers with an industrial EVATEC Clusterline®-200 machine. The single target used for KNN deposition was a 4", stoichiometric $K_{0.5}Na_{0.5}NbO_3$ target bought from JX Nippon Mining & Metals. Growth was achieved by radio-frequency (RF) confocal sputtering at 500 °C in argon atmosphere. The KNN films were grown at three different argon flows, i.e. 30 sccm, 60 sccm, and 90 sccm that will be addressed as low (KL), medium (KM), and high flow pressure (KH) regimes during the analysis. We fabricated KNN films with a thickness spanning from 350 nm (high pressure regime) to 400 nm (low pressure regime). KNN was grown on $Pt(111)/TiO_2/SiO_2/Si(100)$ templates. As top electrode, 30 nm of Pt were grown on all wafers after KNN deposition. The as-deposited KNN films were amorphous. Hence, the wafers were annealed to promote crystallization in a quartz tubular furnace (Carbolite Gero KST 12/600). Samples from all three different pressure-regimes were annealed at 500 °C, 600 °C and 700 °C for 2 h in a semi-open $N_2 + O_2$ atmosphere. The growth and annealing conditions, together with the names of the films, are summarized in Table 1.

For crystallographic characterization, we utilized a Rigaku SmartLab XE X-ray diffraction system, equipped with a copper (Cu) anode of 1.5406 Å X-ray radiation. To assess the ferroelectric properties and leakage currents in KNN films, square platinum (Pt) contacts measuring 200 μm x 200 μm were fabricated using maskless lithography and ion beam etching. The ferroelectric properties were characterized using an aixACCT's TF Analyzer 2000 instrument. Dynamic Hysteresis Measurements (DHM) and Positive-Up Negative-Down (PUND) software modules were used. Leakage currents were evaluated using a Keithley 2612 System voltage source on a SUSS MicroTec PM5 Probe Station. The measurements were made by applying bipolar sweep pulses ranging from −5–5 V. A scanning electron microscope (SEM) LEO 1525 was used to image the surface and cross-section of the films. A quantitative composition analysis of the processed films was done with a Bruker Quantax energy dispersive x-ray spectroscopy system (EDS). To understand the relationship between morphology of the films and their conductivity, Atomic Force Microscopy (AFM) and Conductive Atomic Force Microscopy (C-AFM) measurements were done with a NX10-AFM from Park Systems. Moreover, to assess the local switching properties, local IV curves were taken in regions of the samples with different morphologies and compositions.

Table 1
Growth, annealing conditions, and resulting thickness of RF-sputtered films. The acronyms KH, KM, and KL represent KNN films grown at relative high, medium, and low argon pressure, respectively.

Sample code	Annealing temperature (°C)	Ar flow (sccm)	Growth temperature (°C)	Thickness (nm)
KH	500	90	500	350
	600			
	700			
KM	500	60	500	400
	600			
	700			
KL	500	30	500	400
	600			
	700			

DFT simulations were performed with the Vienna Ab-initio Simulation Package (VASP) [23] using the PBEsol exchange-correlation functional [24]. Projector-augmented wave (PAW) [25] pseudopotentials were used, with the following valence states: K 3 s,3p,4 s; Na 2 s,2p,3 s; Nb 4p,5 s,4d; O 2 s,2p. In all the systems, the kinetic energy cutoff was set to 800 eV and the Brillouin zone was sampled with a 3x3x4 k-point mesh. The chemical disorder on the A sublattice was modelled by means of the Special Quasirandom Structure (SQS) technique [26] as implemented in the software ICET [27]. For each fixed η, the system having *x* atoms of Na and *y* atoms of K and its mirror image share the same SQS supercell (with the two species exchanged) and thus the same randomness. Different SQS were necessarily generated for different values of η. The cluster expansion, common to all systems, was constructed with cutoffs (13 Å for doublets, 8.5 Å for triplets) chosen such that the number of effective cluster interactions be in the order of 40. The initial lattice parameters were prepared according to the Vegard law as a linear interpolation between the (suitably multiplied) equilibrium values of $KNbO_3$ and those of $NaNbO_3$, as obtained in separate simulations for their tetragonal unit cells ($KNbO_3$: a = 3.973 Å, c = 4.053 Å; $NaNbO_3$: a = 3.918 Å, c = 4.021 Å). All systems were then fully optimized to their own equilibrium structure. Convergence threshold for energies were set to 10^{-6} and 10^{-4} eV concerning electronic and structural optimization, respectively, which yielded residual forces no larger than 0.03 eV/Å.

3. Results

3.1. Crystalline phases, orientations, and spurious phases

Out-of-plane XRD measurements were done for KNN films grown at different Ar pressures and annealed at temperatures of 500, 600 and 700 °C. Conditions were summarized in Table 1. Fig. 1 shows the corresponding diffractograms. Overall, several reflections coincide with the ABO_3 structure of KNN's perovskite phase, and the films are {001} preferentially oriented. In most cases, however, the peaks are broadened, pointing out to a mixture of (001) and (100) orientations, i.e. crystallites of the perovskite with long-*c* axis oriented both in plane and out of plane. The *c*-axis (001) is regarded as the polar direction of perovskites in orthorhombic and tetragonal phases [3,28]. From the XRD diffractograms, the appearance of double peaks at 2θ = 22° and 46° related to (001)/(100) and (002)/(200) orientations depends on the deposition conditions and on the annealing temperature. For the

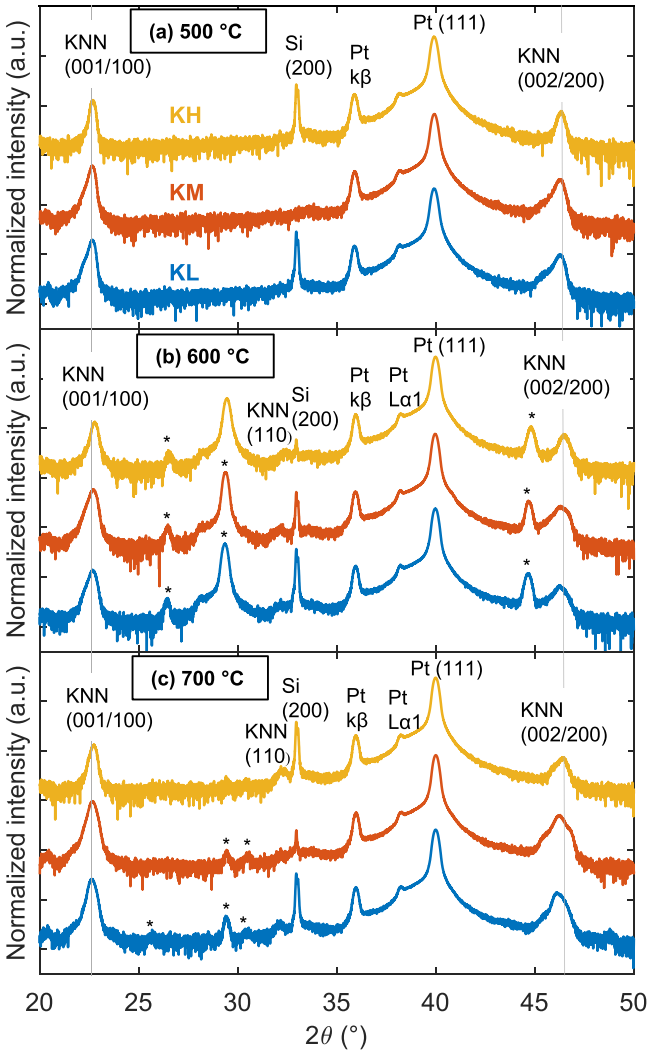

Fig. 1. Symmetric XRD θ-2θ plots of KNN films grown at high (yellow), medium (red) and low (blue) Ar flows and annealed at a) 500 °C, b) 600 °C or c) 700 °C. The intensity is in logarithmic scale, and it was normalized to the thickness of the films. The asterisks mark the peaks related to spurious pyrochlore phases in KNN films.

high-pressure regime (KH), a (100) almost-single peak is observed for annealing temperatures of 500 °C and 600 °C, while a (001) shoulder to the left appears at 700 °C. In addition, for the KH condition, the XRD intensity of {001} reflections is rather low, which might point out to a reduced crystallinity and/or small crystallites. The structural quality at higher argon (Ar) flow can be attributed to a low energy of Ar ions at higher pressure regime, which results in limited diffusivity of the sputtered elements. Consequently, the atoms attain a short-range arrangement and crystallinity is low. Under conditions of high Ar flow, growth rate estimations indicate that we are not operating within the minimum zone of the Paschen curve [29]. When the Ar flow is too high, the increased collision rate between Ar atoms reduces the mean free path of the sputtered atoms. This reduction in the mean free path leads to lower sputtering efficiency compared to lower pressure regimes (KL), causing atoms to impinge on the substrate with reduced momentum. Consequently, a substrate temperature of 500 °C under high-pressure plasma conditions, followed by annealing temperature of 500 °C are insufficient to induce extensive crystallization in the film. In contrast, for medium (KM) and low-pressure regimes, the structural quality improves since the Ar plasma is more energetic. The {001} diffraction achieves higher counts per second and the reflection attributed to polar (001) orientation becomes present for all annealing temperatures.

Fig. 2a shows the dependence on the annealing temperature of thickness-normalized intensity of the (001)/(100) reflection for different Ar flows. The dependence is weak for the KH regime as the intensity of (001)/(100) remains, overall, constant. Nevertheless, for KM and KL pressure regimes, a minimum point at 600 °C and then a substantial increase at 700 °C are found. The general trend is consistent with an expected increase in crystallinity at more energetic conditions. Interestingly, the highest intensities are found for medium pressure deposition and high temperature annealing, signaling a more balanced grain nucleation and growth. The out-of-plane *c*(001) and *a*(100) lattice parameters as a function of increasing deposition pressure and annealing temperature were calculated and they are displayed in Fig. 2b. The values were estimated from the deconvolution of the (100) and (001) peaks. The *a* and *c* lattice parameters show a net increase at 700 °C, while a minimum at 600 °C can be spotted for all three regimes. Moreover, the values are also dependent on the deposition pressure as the largest increases are found for the low-pressure regime. This might be related to a more energetic plasma in, otherwise, analogue conditions. For ferroelectric perovskite films, the enlargement of the out-of-plane lattice parameter is important because it can give rise to a reordering from the non-polar (100) orientation, to the polar (001) one [9]. Regarding crystallinity and (001) orientation of the KNN perovskite cell, our results suggest that deposition in low pressure conditions and a high

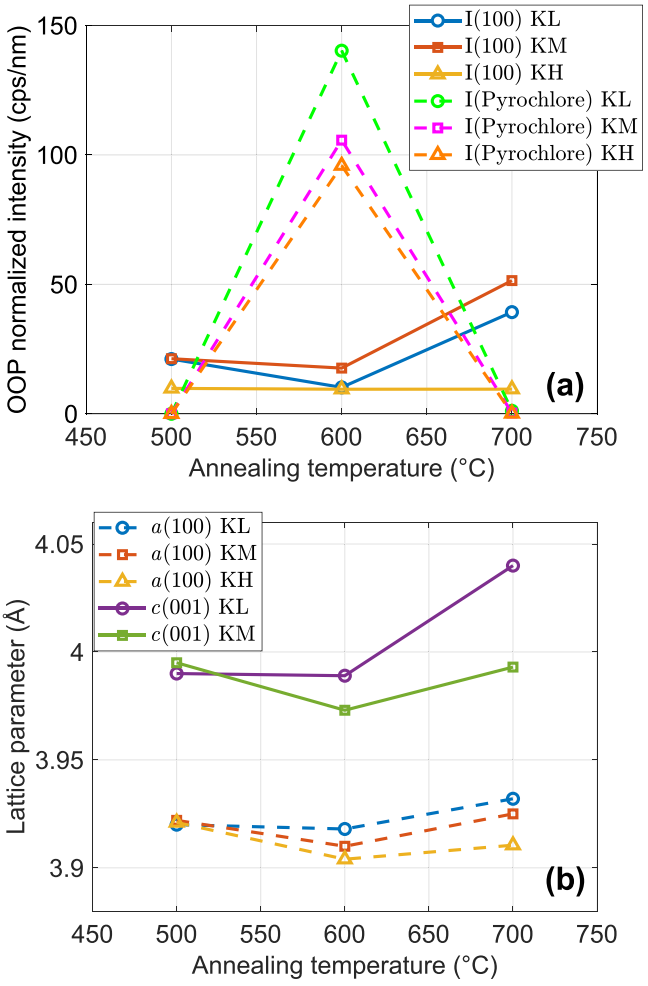

Fig. 2. (a) KNN {001} and pyrochlore peak intensities (I) normalized (cps/nm) to the thickness of the KNN films for KL (30 sccm Ar), KM (60 sccm Ar) and KH (90 sccm Ar) growth conditions. (b) Out-of-plane a and c lattice parameters as a function of annealing temperature. The c(001) of KH is not present, as it is predominantly (100) oriented.

annealing temperature of 700 °C are beneficial. It must be noted, nevertheless, that reported values of *a*-axis for bulk KNN in pseudo-cubic structure are around 3.94 Å, while reported values for the *c*-axis are around 4.016 Å [30]. Thus, in comparison, all our KNN films exhibit lower lattice parameters values. The lower values can be ascribed to in-plane tensile stress of the perovskite cell due to the substrate, or to the loss of alkali ions during deposition and annealing [9].

Further analysis of Fig. 1 reveals that the perovskite (001)/(100) and (002)/(200) reflections are not the only signals present in our KNN films. Even though only Pt (111) and {001} perovskite-related reflections are all present in the diffractograms at annealing of 500 °C, at 600 °C and 700 °C, evidence of (110) orientation of perovskite KNN is also found but with small intensity ($2\theta = 32°$). More importantly, however, a pyrochlore spurious phase with high crystallinity is found at $2\theta = 29.4°$ when KNN films are annealed at 600 °C. Unexpectedly, the signal is even higher than the {001} reflection of the perovskite-KNN and confirms the presence of a pyrochlore phase in our KNN films. Interestingly, the spurious phase also seems oriented with regards to Pt (111), as polycrystalline pyrochlore phases should display several reflections in the range of our XRD measurements. Pyrochlore phases can exist in several compositions like $A_4Nb_6O_{17}$, $A_2Nb_4O_{11}$, $A_2Nb_6O_{16}$, $A_2Nb_8O_{21}$, etc., where A can represent Na, K, or a stoichiometric combination of both [31,32]. A common feature of spurious phases is that they are all alkali and oxygen deficient when compared to desired perovskite $ANbO_3$ phases. In Fig. 2a, the intensity of crystalline pyrochlore phase is shown with respect to deposition pressure and annealing temperature. At 500 °C there is no evidence of it and at 700 °C there are just minor indications. At 600 °C, however, their high presence coincides with an intensity drop from (001)/(100) reflection of the KNN perovskite phase and with an inflection point for the lattice parameters of Fig. 2b. Moreover, the pyrochlore is even more present for low pressure growth conditions of KNN.

The coexistence of perovskite and pyrochlore phases has been studied in detail for PZT ferroelectrics. It has been shown that Pb-deficient phases are more stable below 650 °C, while the perovskite becomes relevant at high temperatures, when oxidation is extensive and it stabilizes the ABO_3 composition [33,34]. In the field of PZT, a pyrochlore to perovskite transformation during annealing is achieved by increasing processing temperature and by adding excess PbO to the mixture films during growth or processing [35]. Like K and Na, Pb can evaporate from films in the form of volatile oxides. For our KNN films, the pyrochlore is highly favored at 600 °C, but transforms to the perovskite at 700 °C. Nevertheless, in this study, we have not used excess alkali to compensate for a full phase transformation and thus the perovskite forms at the expense of the pyrochlore phase. We will discuss later on the dynamics and chemical nature of the perovskite and

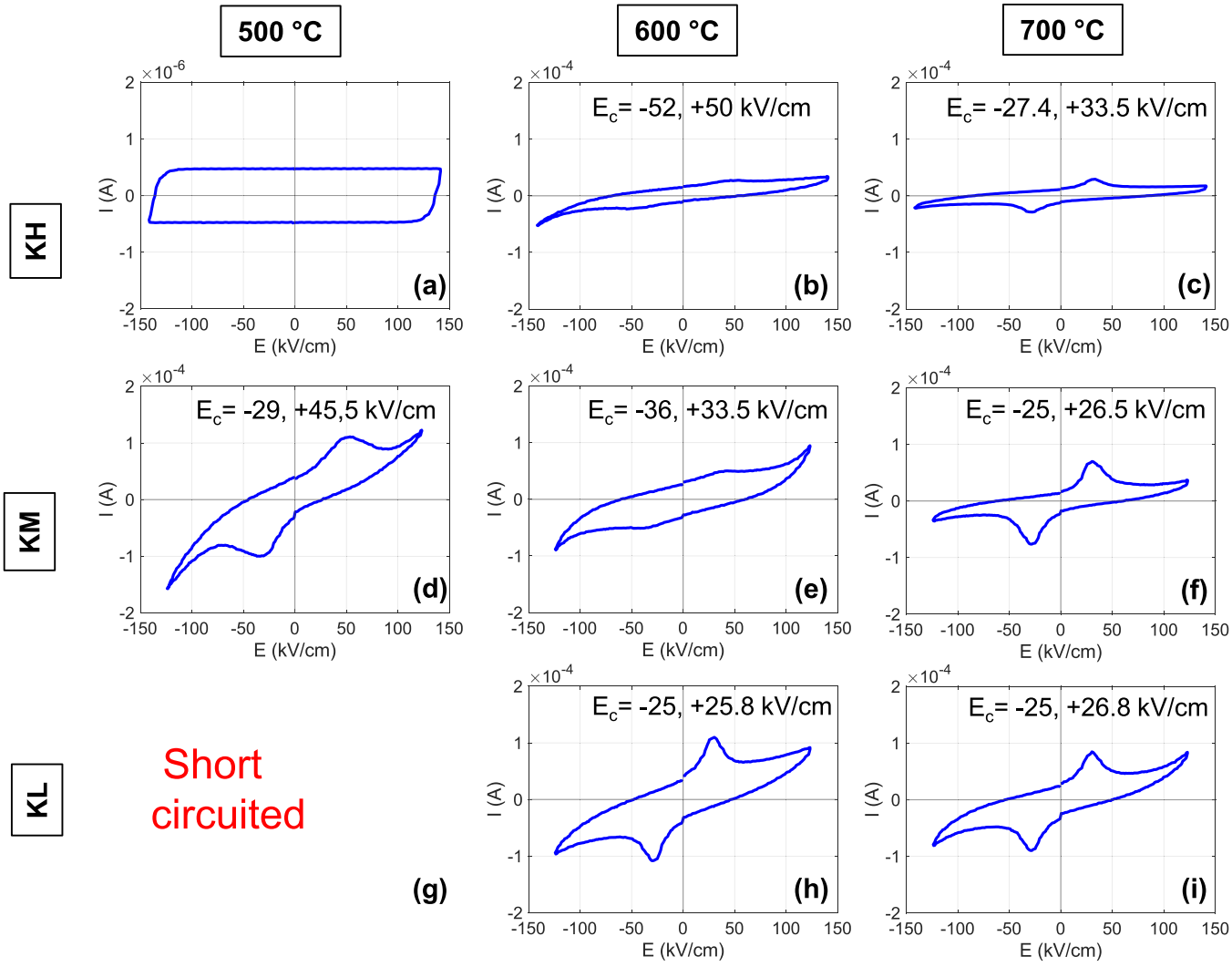

Fig. 3. Current – electric field characteristics of KL, KM, and KH films annealed in N_2+O_2 at different temperatures. On the y-axis, deposition pressures: (a, b, c) grown with 90 sccm of Ar; (d, e, f) with 60 sccm; (g, h, i) with 30 sccm. On the x-axis, annealing temperatures in N_2+ O_2 atmosphere: (a, d, g) annealed at 500 °C; (b, e, h) at 600 °C; (c, f, i) at 700 °C.

spurious phases of KNN caused by segregation.

3.2. Leaky ferroelectric KNN capacitors

Since mixed (001)/(100) orientation for perovskite KNN films was observed, some ferroelectric behavior was expected. Thus, Dynamic Hysteresis Measurements (DHM) were performed by applying triangular ± 5 V signals at 1 kHz to the top Pt electrodes of the samples. The current vs electric field characteristics are reported in Fig. 3. Different deposition conditions and annealing temperatures produced varying electrical responses from the KNN films. Except for only-capacitive KH-500, and for short-circuited KL-500, all prepared films behaved like leaky ferroelectric capacitors with evident switching peaks [36].

For KH-500 (Fig. 3a), even though a distinctive capacitive behavior is observed, its reduced capacitance (look at *y*-scale) points to a low-k insulator with dielectric constant of 10. Such value deviates from the high-*k* values typically observed for perovskite KNN, spanning from around 200–1200 [32,37–39]. This is further supported by XRD, where low crystallinity was observed. Similarly, low *k*-values can be inferred from the narrow current loops in Fig. 3b and c, corresponding to samples deposited at KH conditions and annealed at 600 and 700 °C. Yet also small ferroelectric switching peaks are found in the loops of these samples accompanied by evidence of leakage. More favorable conditions for ferroelectricity are found when the sputtering pressure is reduced and the annealing temperatures are increased. The more prominent switching peaks are those obtained for films deposited at low pressure and annealed at 600 and 700 °C (Fig. 3h, i). As the (001) oriented perovskite should give rise to a polarization in the out of plane direction, the ferroelectric switching responses from samples grown at KM and KL conditions are consistent with the mixtures of (001)/(100) orientations found in XRD of Fig. 2a. Moreover, the increased ferroelectric responses also are in correspondence with larger out-of-plane *c*-lattice parameters [28,40].

To reduce the large effect of leakage on polarization measurements, we performed positive-up negative-down (PUND) measurements for the KL-700 sample. The polarization-electric field hysteresis loop is reported in Fig. 4. Asymmetric polarization with $P_{r+} = 12.7$ μC/cm^2 and $P_{r-} = 8.5$ μC/cm^2 (2Pr of 21.2 μC/cm^2) was estimated. While polarization values of our KNN film are lower than those reported in literature for optimized KNN films (20–25 μC/cm^2 [39,41]) the coercive fields instead align well with reported values [39,42,43].

Leakage measurements were done by using a bipolar, triangular ± 5 V signal (± 3 V for KL-500 that showed exceptionally high leakage). Analysis performed on the KNN films annealed at 500 °C are displayed in Fig. 5 (other annealing temperatures are included in supplementary material). It is evident that leakage decreases dramatically

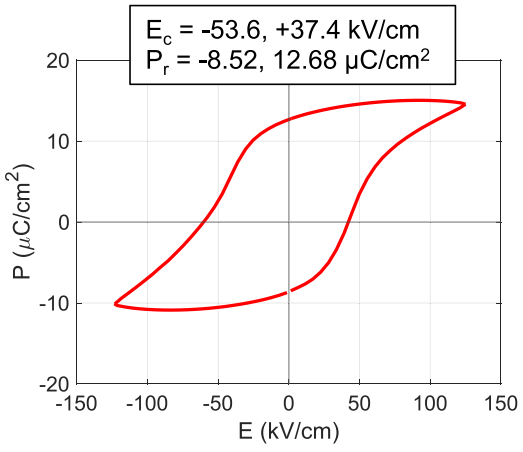

Fig. 4. P-E hysteresis loop obtained by PUND method for a KNN film grown with Ar flow of 30 sccm (KL) and annealed at 700 °C in N_2+O_2 atmosphere.

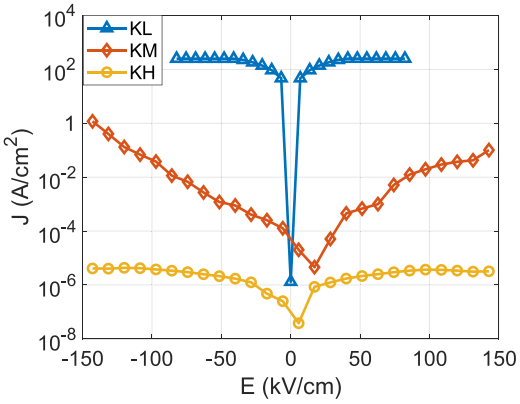

Fig. 5. Leakage current density as a function of the electric field in KL (30 sccm), KM (60 sccm) and KH (90 sccm) films annealed at 500 °C.

from deposition at low pressure (30 sccm of Ar) towards higher pressure (90 sccm of Ar). The values confirm both the insulative behavior of KH-500 and the short circuit produced in KL-500. Therefore, even though energetic deposition of KNN in low Ar conditions produces higher crystallinity and bigger lattice parameters for the perovskite phase, it also brings about higher leakage currents. In previous studies, we discussed how oxygen and alkaline vacancies produced at high plasma energies and high annealing temperatures largely contribute to leakage in KNN films [8,9]. Furthermore, leakage in the present paper can also be attributed to gross morphological defects resulting from phase segregation that in turn depend on growth and annealing conditions [8].

3.3. Morphology of films

Fig. 6 shows the morphology of KNN films obtained from SEM measurements as a function of Ar pressure during sputtering deposition and annealing temperature. At high pressure (high Ar flow) and annealing temperature of 500 °C, a uniform, continuous film is observed (Fig. 6a). However, the morphology becomes uneven for higher annealing temperatures, and it is significantly affected in KNN films deposited at low pressure and high temperature (Fig. 6e, f, h, i). As introduced in the previous section, despite the flat morphology and low leakage of KH-500, it also comes with low crystallinity, lack of (001) orientation, no ferroelectricity, and low-*k* value. Some of these characteristics cannot be attributed to a proper perovskite phase.

In SEM images (Fig. 6a and d), small white dots can be found for high pressure and low temperature annealing conditions. The nucleation sites soon evolve into circles that grow radially away from the center in films annealed at higher temperatures. These effects are ever more present in KNN films deposited at lower pressures and high annealing temperatures. Beyond the circular regions, the surrounding material acquires an irregular morphology, with evidence of pinholes, cracks, and general physical degradation. In the next section, we will show how such a microstructure is related to chemical segregation in the films. Due to their distinct shape, and reminiscence of collapsed volcanic cones, the circular features observed in our KNN films have been termed "volcanoes". Fig. 7a shows a typical volcano feature: it has a central "crater", which is characterized by a rough morphology. Also, the film develops stripes in all directions away from the crater (Fig. 7b), ranging from as small as 2–3 μm, to as large as 70 μm. Surrounding the crater, the "flanks" of the volcano are raised, forming elevated borders around the circular defects (cross section image in Fig. 7c). From such a micrograph, it arises that volcanoes represent an accumulation of material with crystalline characteristics. They act as nucleation growth centers where the crystalline KNN perovskite phase starts to develop and grow, recruiting alkali elements from peripheral areas to achieve the ABO_3 composition (demonstrated in the next section). The volcanoes are

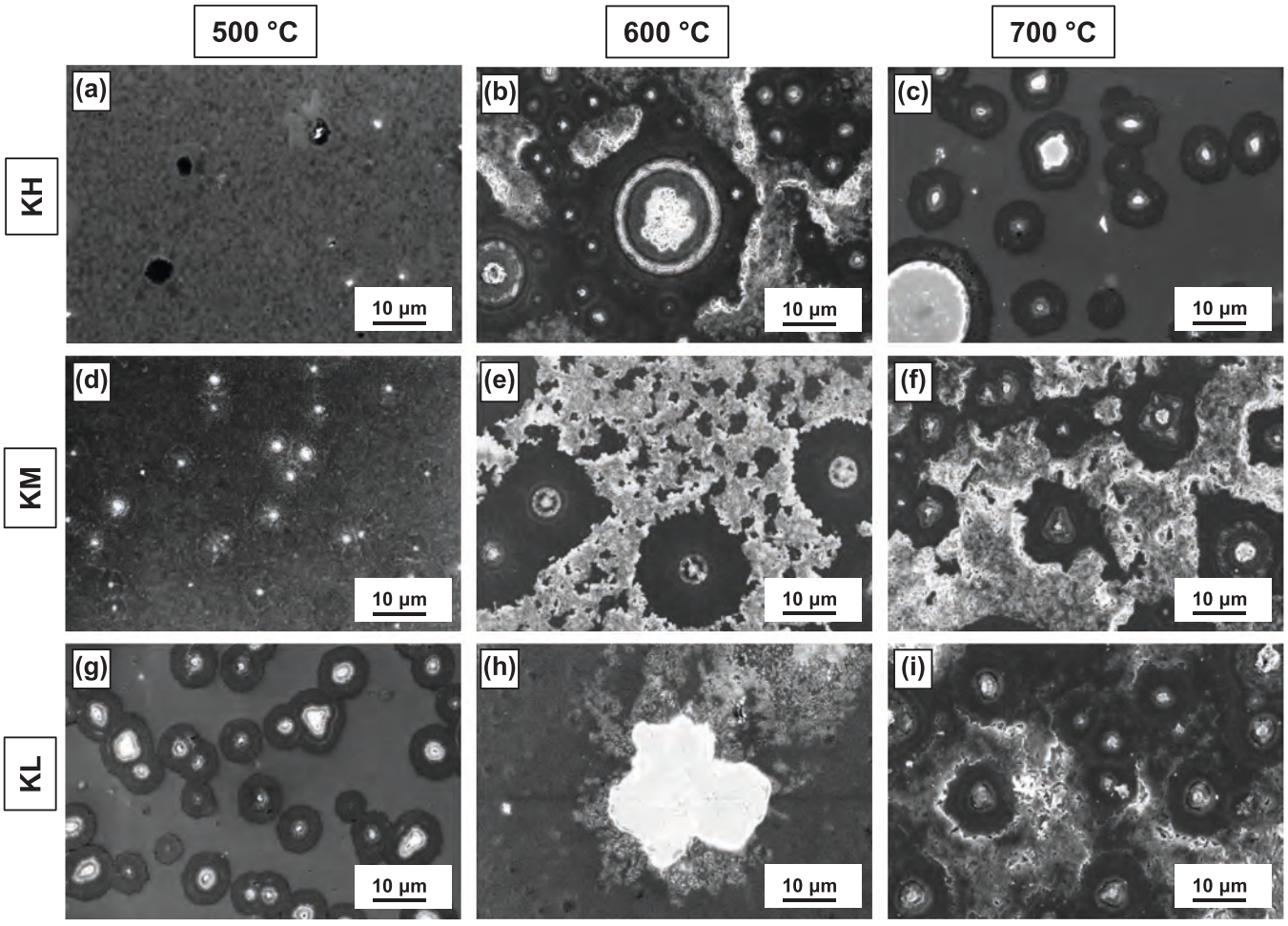

Fig. 6. Morphology SEM images of KL, KM and KH films annealed at 500, 600 or 700 °C in N_2+O_2 atmosphere. On the y-axis, deposition pressures: (a, b, c) grown with 90 sccm of Ar; (d, e, f) with 60 sccm; (g, h, i) with 30 sccm. On the x-axis, annealing temperatures in N_2+ O_2 atmosphere: (a, d, g) annealed at 500 °C; (b, e, h) at 600 °C; (c, f, i) at 700 °C.

bigger and more numerous for KNN films grown at low pressure and annealed at high temperatures. This also coincides, in general, with higher crystallinity and ferroelectricity observed for films prepared in the mentioned conditions. The regions surrounding the volcanoes, however, acquire a degraded morphology. Fig. 8 shows how such alkali deficient regions can change with increasing annealing temperature for a KNN film deposited at low pressure. At 500 °C (Fig. 8a), the area is uniform and presents itself with few crystallites. At 600 °C (Fig. 8b) the film crystallizes better and thus shows several crystalline cubes (it is also at 600 °C that a large increase of a pyrochlore phase is observed in XRD measurements). At 700 °C (Fig. 8c), the cubes seem bigger, but the material also suffers extensive degradation due to mass migration towards the volcano features. According to film composition analysis, the degradation corresponds to phase segregation in the KNN films, as it will be explained next.

3.4. Segregation of Na and K in KNN films

We performed Energy-Dispersive X-ray Spectroscopy (EDX) analysis on all samples annealed at various temperatures. Our analysis focused on overall and local elemental distributions of sodium (Na), potassium (K), and niobium (Nb) within the KNN films. Oxygen (O) was also considered but only qualitatively because EDX is less accurate for low-mass elements. For this section, due to strong segregation effects but higher ferroelectric response, KNN films deposited at low pressure were taken as detailed analysis example. A full scenario of segregation of phases for all films can be found in the Supplementary material. Fig. 9a shows elemental distribution maps for Nb, Na, and K in a large area of a KNN film annealed at 700 °C (KL-700). While Nb seems to be homogeneously distributed on the substrate, Na and K elements are not. Visibly, Na-rich, yet K-deficient, islands are observed in the image. These Na-rich, K-deficient regions correspond exactly to the volcano features found in morphological analysis (Fig. 9b top). The accumulation of sodium and depletion of potassium that characterizes the volcanoes is also evident when looking at an elemental line scan across one of these features (Fig. 9b down). It is obvious that within the volcano region there is an accumulation of Na, and a spike of O and Na at the very center. This is accompanied by a depletion of K in the volcano. At the very center of the volcanoes, the increase of oxygen and sodium points out to a sodium oxide phase, which might be acting as nucleation center for the growth of the Na rich perovskite phase.

Fig. 10 shows elemental atomic ratios between K, Na, and Nb across three different regions of films deposited at low pressure and annealed at various temperatures: 1) overall region comprehending whole SEM-EDX area of around 1 mm× 1 mm (green lines); 2) Na-rich, K-deficient volcanoes (blue lines); and 3) peripheral areas of the volcanoes (magenta lines). Ideally, the (Na+K)/Nb ratio in zone 1 (whole area) would be expected to be one, denoting a fully stoichiometric, perovskite $K_{0.5}Na_{0.5}NbO_3$ film. Instead, the green line in Fig. 10a shows a (Na+K)/Nb < 1 for all annealing temperatures, thus evidencing a general loss of alkali elements. While undesired, this is a common feature of KNN [10,44,45]. Interestingly, the retention/loss of alkali elements seems to have

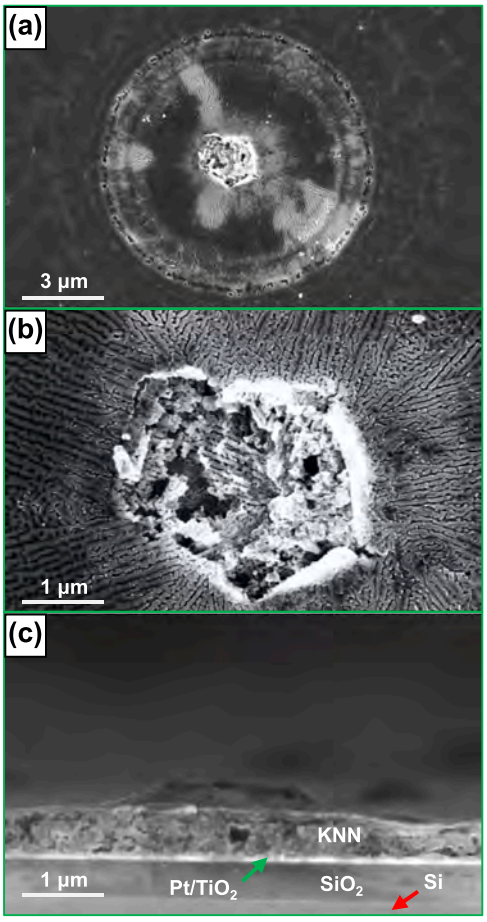

Fig. 7. SEM images taken from sample KM annealed at 600 °C. (a) Volcano defect (b) close-up on the volcano's center (c) cross section of the film with a volcano defect.

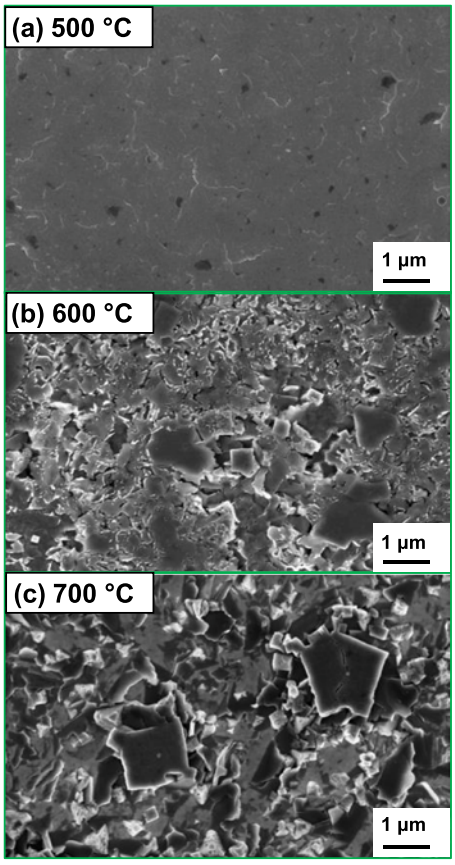

Fig. 8. SEM morphology of the alkali deficient region in a KM film annealed at (a) 500 °C, (b) 600 °C, (c) 700 °C.

opposing behaviors for higher annealing temperatures. While the (Na+K)/Nb ratio remains somewhat constant at around 0.8, the Na/K ratio (which should also be ideally of one for $K_{0.5}Na_{0.5}NbO_3$), increases above one by increasing the annealing temperature (Fig. 10b). This is not simply due to a higher evaporation rate of K in comparison to Na (which is true anyway), but because of an enhanced retention of Na with increasing temperature (Fig. 10c), and concomitant faster loss of K in the overall film (Fig. 10d). This finding might seem counterintuitive for Na, as annealing temperature is expected to assist the evaporation of both Na and K in the form of oxides. Nevertheless, the annealing of our KNN films is performed in parallel and not in sequence, for which results cannot be regarded as chronological in nature. Therefore, the Na/K ratio shows that, starting from the same KNN films, higher annealing temperature ensures a better retention of Na but further loss of K. The effect might be related to a higher ionization energy of Na compared to K [46] and enhanced by higher diffusivity and reactivity of oxygen at higher temperature. Oxygen would compensate for oxygen vacancies produced during deposition at low pressure [47]. The varying elemental mass loss also reflects in the segregation of the elements as obtained from local EDX measurements.

In region 2 (Na-rich, K-deficient volcanoes), marked with blue color in Fig. 10a, the (Na+K)/Nb ratio is close to one, which is expected for a proper perovskite phase with stoichiometric values for all elements. This in turn confirms a mass diffusion of alkali elements toward the volcano features. Yet, the migration is highly uneven because the Na/K (Fig. 10b) ratio is well above 1 for all annealing temperatures, increasing above 3 by raising the annealing temperature. This can also be corroborated by the increasing Na/Nb ratio of Fig. 10c, and by the decreasing K/Nb ratio in Fig. 10d. It becomes thus clear that Na is easily diffusing/segregating and forming Na-rich circular regions, while K is both diffusing away from the volcanoes and being lost to evaporation faster than Na. It is interesting, however, that in the volcano region the chemical proportions of elements are fairly constant, lying between $K_{0.3}Na_{0.7}NbO_3$ and $K_{0.21}Na_{0.79}NbO_3$. In this regard, EDX results suggest that a Na-rich $K_xN_{1-x}NbO_3$ ($x < 0.5$) composition could be chemically and thermodynamically more stable when deposited by RF sputtering than the commonly reported $K_{0.5}Na_{0.5}NbO_3$ composition. This is coherent with previous studies where other morphotropic phase boundaries of $K_{0.17}Na_{0.83}NbO_3$ and $K_{0.35}Na_{0.65}NbO_3$ were found to be beneficial for KNN-based systems [20,22]. On a related note, it is also important to state that in the centers of large volcanoes, particularly in those observed in the KL-700, stress occasionally leads to cracking. For large volcanoes, the center often appears as holes consisting entirely of silicon oxide, indicating that even the platinum seed layer was removed due to the induced built-in stress, coinciding with larger *c*-lattice parameter in the out-of –plane direction.

For region 3 (periphery of volcanoes), marked by magenta lines in Fig. 10, the situation is decisively different. The reduced ratios of (Na+K)/Nb = 0.59 ± 0.01 for 500 °C, 0.56 ± 0.06 for 600 °C, and 0.58 ± 0.07 for 700 °C of annealing temperature (Fig. 10a) show a general deficiency of alkali elements in these areas. Moreover, regarding annealing temperature, the (Na+K)/Nb ratio remains fairly constant. Nevertheless, magenta lines in Fig. 10b, c, and d show that, in region 3, potassium exists in major proportion with respect to sodium. Yet, this cannot be regarded as a K-rich perovskite region because, in any case, considering a composition of $K_{0.5}Na_{0.5}NbO_3$, the K/Nb ratios remain always under stoichiometric (< 0.5). As mentioned earlier, all pyrochlore phases are alkali-deficient, thus it is logical to think that in region 3 a K-rich pyrochlore phase develops. The elemental ratios in these

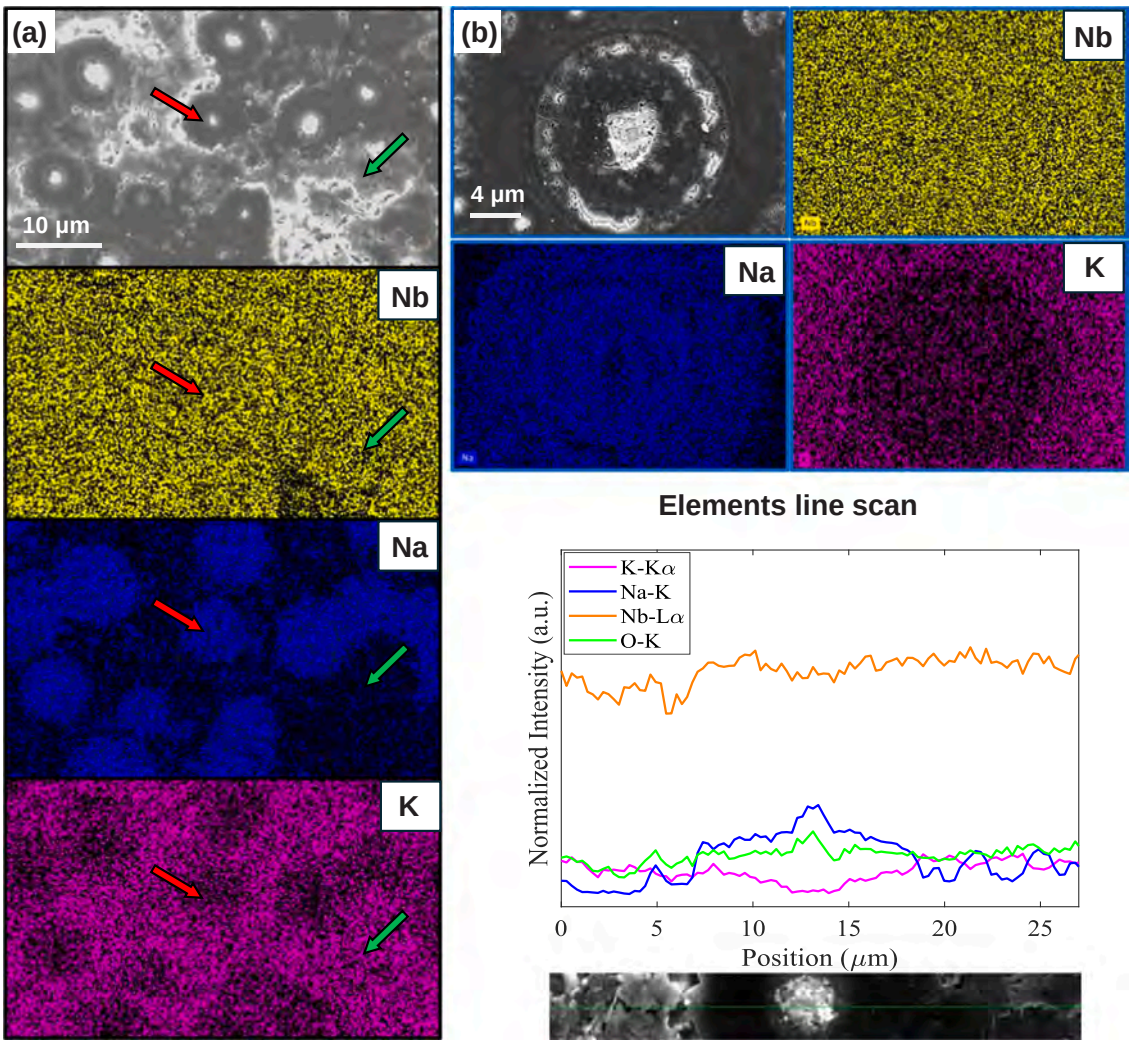

Fig. 9. (a) elemental EDX maps of Na, K, and Nb of a large area of sample KL 700. The red arrow is pointing to the same Na-rich volcano region in every image, while the green at an alkali deficient region (volcanoes periphery). (b) Top image, EDX line scan of K, Na, Nb of a volcano and surrounding regions; bottom image, elemental maps of Na, K and Nb for a single volcano feature.

zones of our films are close to a pyrochlore composition of $A_4Nb_6O_{17}$, where A = K+Na and A/Nb = 0.67 [18,48,49].

General compositional analysis for the other two pressure growth conditions is shown in Table 2. Even though the physical and chemical behavior of KNN films grown under varying argon flow was similar, better (Na+K)/Nb ratios were obtained for lower deposition pressures. Other than the expected higher plasma energy at low pressure, a higher mass transfer rate from target to wafer also occurs (Table 2). Both conditions might reduce the loss of alkali elements resulting in a (Na+K)/Nb ratio closer to the perovskite ratio. On the contrary, lower plasma energy and higher deposition pressure reduce the efficiency of mass transfer and allow for significant alkali loss. The (Na+K)/Nb = 0.65 ratio in the last case is closer to that of a pyrochlore phase, which would produce no ferroelectric response and low-k values (indeed observed for KL-500 in Fig. 3a).

The analysis of the various regions highlights that, on the whole film, there is a high deficiency of K. This can be explained by a higher vapor pressure of K with respect to Na [50]. Therefore, K evaporates faster than Na during deposition, and even more easily at high annealing temperatures. Locally, however, the loss of K, and of Na to a minor extent, leads to the formation of undesirable pyrochlore phases in the films. Yet, while K is lost during the entire process, Na migrates and accumulates forming nucleation centers and a chemically more stable Na-rich KNN perovskite phase. These perovskite regions take the form of volcanoes that might suffer from increased stress leading sometimes to delamination at the center of the features. Regarding the alkali-deficient regions, depending on KNN growth and annealing conditions, they can suffer from structural failure of the material. In Fig. 11a and b, an EDX compositional map overlayed on a SEM image is displayed. The sample has been patterned by lithography, developed in aqueous TMAH base, and etched by ion beam etching to define individual top Pt electrodes. The Pt region on the right of the images corresponds to a section of the top metal layer. In general, the Na-rich perovskite regions (volcanoes) are stable and survive well the lithographic processes (Fig. 11a). Nevertheless, the alkali-deficient zones are subject to physical degradation upon exposure to basic aqueous environment (more dramatic for films annealed at 700 °C). This is evident when looking at the Nb signal in Fig. 11b, where Nb is maintained in the perovskite islands, but eroded away completely in the alkali-deficient areas. Beneath the platinum top Pt-electrode, which serves as a protective capping layer, the film maintains mass-integrity yet displaying phase segregation. The findings strongly indicate that a larger Na/K ratio could lead to KNN films with increased chemical stability and limited segregation. Indeed, a practical, ferroelectric 70/30 Na/K composition for KNN has already been reported in literature for KNN films [20,22].

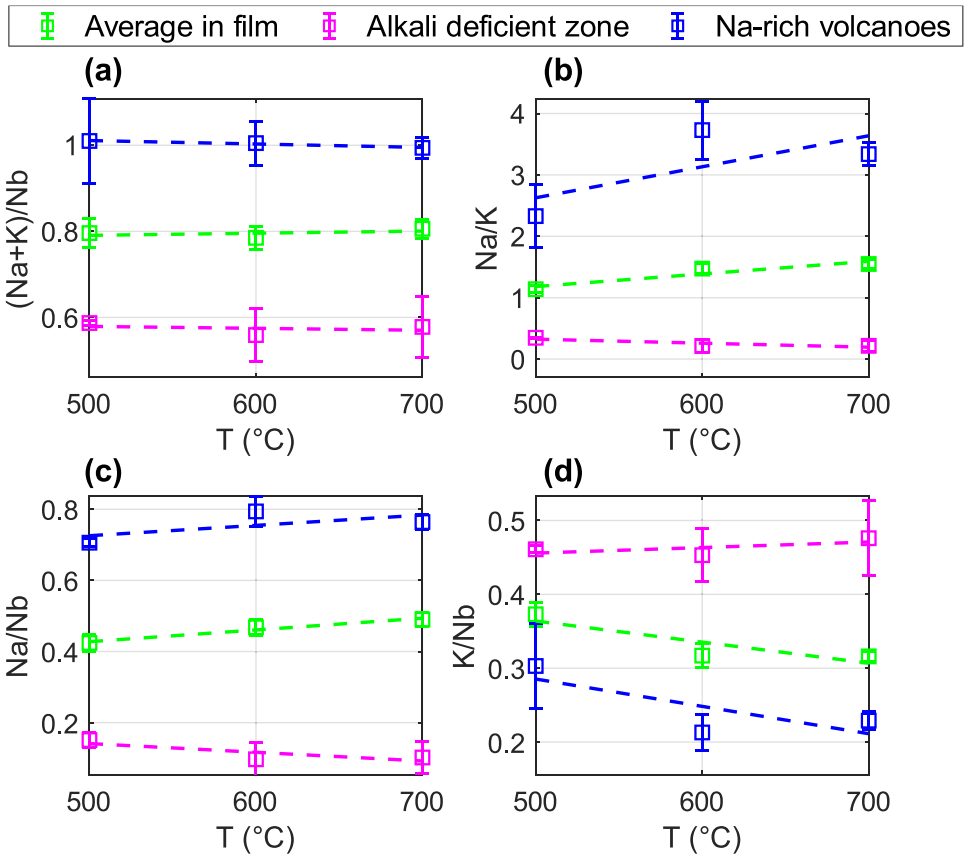

Fig. 10. a) (K+Na)/Nb, (b) Na/K, (c) Na/Nb and (d) K/Nb atomic ratios for the sample KL at different annealing temperatures. In green, the average films composition (region 1); in blue, the Na-rich volcano zone (region 2); in magenta, the alkali deficient K-rich zone (region 3).

Table 2
General (Na + K)/Nb ratios found for KNN films grown at different Ar flows and annealed at different temperatures.

Ar flow (sccm)	Growth rate (nm/h)	(Na+K)/Nb 500 °C	(Na+K)/Nb 600 °C	(Na+K)/Nb 700 °C
30 (KL)	800	0.80 ± 0.03	0.78 ± 0.03	0.81 ± 0.02
60 (KM)	800	0.77 ± 0.01	0.78 ± 0.02	0.82 ± 0.05
90 (KH)	600	0.65 ± 0.02	0.78 ± 0.02	0.78 ± 0.03

3.5. Local electrical response of segregated phases

To further corroborate the perovskite nature of the volcano features in our films, we conducted Atomic Force Microscopy (AFM) and conductive-AFM analysis on a KL-700 sample (Fig. 12a and b, respectively). Areas where both Na-rich perovskite and alkali-deficient pyrochlore phases appear were analyzed. Topography shows that, as was found from cross-section SEM (Fig. 7c) the center regions of the volcanoes are elevated, but the immediate surroundings lie relatively flat. This demonstrates, except for the center of the circular features, a good adherence and stability of the underlying material. Instead, the alkali-deficient areas are rough and, in general, elevated. Some visible cracks even appear in the borders between the two regions, thus indicating poor material coherence. An electrical current map was obtained in the same area by applying a tip voltage during C-AFM measurements (Fig. 12*b*). In general, both the Na-rich perovskite and the alkali-deficient pyrochlore display an insulative behavior, which is, in any case, better for the former. Nevertheless, while the current map is more uniform in the Na-rich region, on the alkali deficient region some localized conduction spots are produced. Some of the spots clearly coincide with morphological features, in particular cracks on the film,

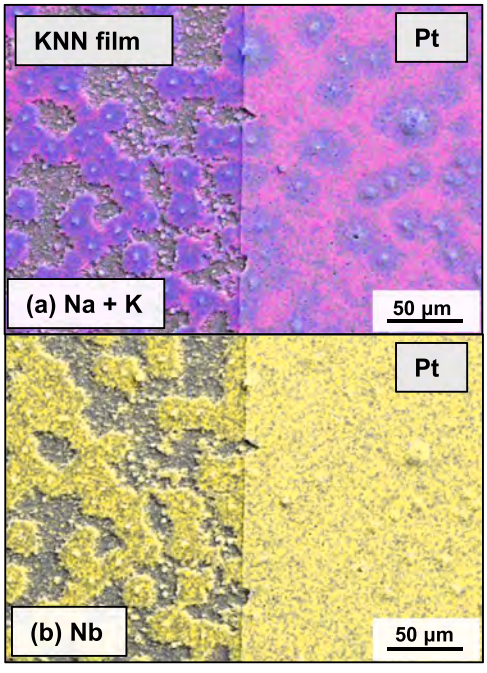

Fig. 11. EDX elemental maps of a) Na (blue) + K (magenta), and b) Nb (yellow) superimposed to the same SEM image of KM-700 film annealed in N_2 + O_2 atmosphere.

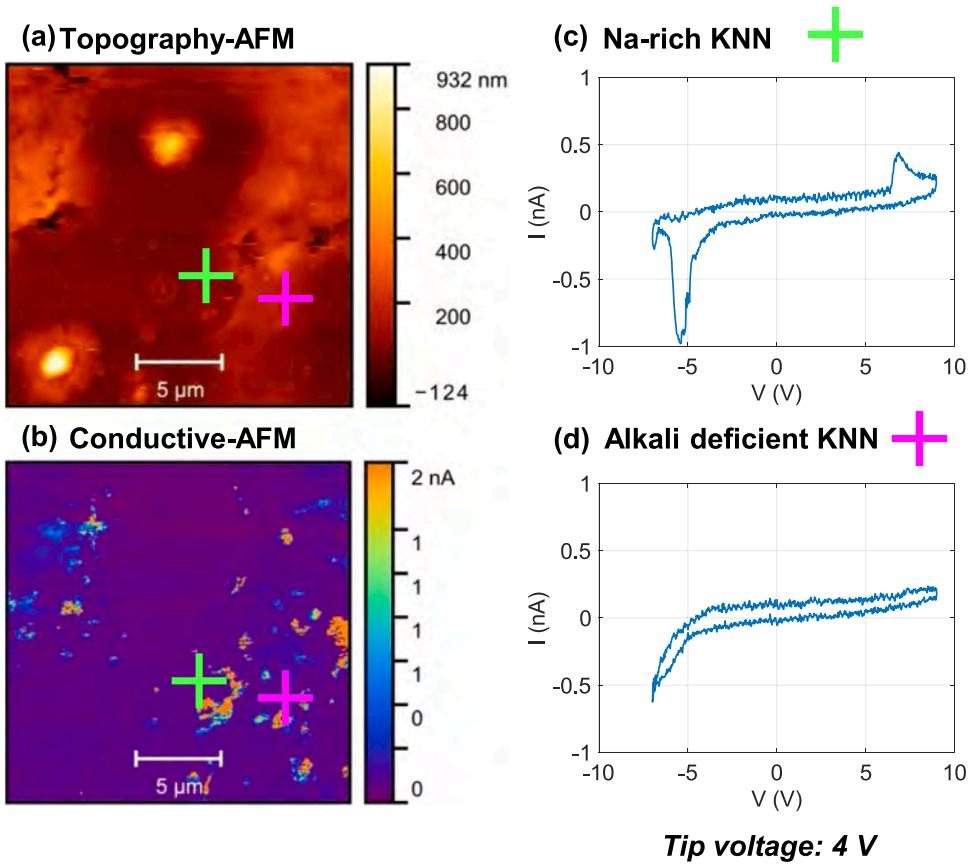

Fig. 12. a) Topography AFM and b) conductive AFM of KL-700. Local I-V measurements on c) Na-rich perovskite and d) alkali deficient regions. The crosses indicate the local I-V measurement positions on the film.

that become paths to conduction towards the bottom electrode. We have, in the past, studied this situation in KNN films deposited by PLD [8]. Local I-V measurements were made in both Na-rich and alkali deficient regions, indicated by green and magenta crosses in Fig. 12b, respectively. Fig. 12c shows characteristic ferroelectric-switching of the Na-rich perovskite. Fig. 12d, instead, shows only a capacitive behavior of the alkali-deficient pyrochlore region, yet with more leakage with an applied negative voltage. Thus, the C-AFM measurements further demonstrate that the Na-rich KNN volcanoes are constituted from a polar perovskite phase of KNN, which is sufficiently insulating. This comes, however, at the cost of segregation, physical damage, and high leakage in the peripheral, alkali-deficient areas.

3.6. DFT calculations

We performed Density Functional Theory simulations with the aim of giving theoretical support to the observed segregation, by means of total energy comparisons. We considered for all our calculations a 90-atom supercell – namely, a 3x3x2 multiple of a 5-atom perovskite unit cell – 18 of which therefore lie on the A-site sublattice (more details to be found in the methods section). Within such common framework, we considered different systems by tuning the relative percentages of Na and K atoms on the A sublattice, with the constraint $N_{Na} + N_K = 18$, to reproduce different concentrations, ranging from the perfectly mixed 50 %/50 % Na/K (9 atoms of each species) to the fully segregated (18 atoms of one species only). In fact, the primary aim of the simulations is to compare the reference case of perfectly mixed 50 %/50 % alloys with the situation in which (full or partial) segregation occurs.

In order to allow for meaningful total energy comparisons, the same number of atoms is required, not only overall, but also species by species. Therefore, for each structure having x atoms of Na and y atoms of K we also considered its mirror image (with y atoms of Na and x atoms of K) and looked at the average of the total energies of these two structures.

Specifically, we considered the total energy difference:

$$\Delta E = E(x,y) - E_0 = \frac{E_{Na=x,K=y} + E_{Na=y,K=x}}{2} - E_0$$

where $E_0 = E_{Na=9,K=9}$, i.e., the energy of the perfectly mixed structure (which by construction needs no mirror image), is chosen as reference. This can be seen as a function of x and y in the range 0–9 for x (or mirrored for y) with the constraint $x + y = 18$ (for each case), or alternatively as a function of the miscibility index (η):

$$\eta = \frac{|x-y|}{18}$$

defined so as to range between 0 (complete miscibility) and 1 (complete segregation).

We considered the two endpoints η = 0 (fully mixed) and η = 1 (fully segregated) together with four different in-between concentrations (η = 0.33, 0.44, 0.55, 0.66). As shown in Fig. 13, ΔE(η) reaches a minimum in the intermediate regime, namely at η = 0.66, which for the Na-rich phase corresponds to Na/Nb and K/Nb ratios of 0.83 and 0.17 respectively, reasonably close to the experimental values shown in Fig. 13.

We remark that our aim here was to target specifically the energy differences induced by the amount of disorder on the A sublattice, neglecting all other non-idealities, such as the onset of a pyrochlore phase in the K-rich systems and the overall deficiency of alkali atoms with respect to Nb (an ideal perovskite structure with tetragonal phase is assumed everywhere). The structural modelling we adopted here is not necessarily guaranteed to reproduce experimental findings accurately. Also, considering the small energy differences at stake, even with a more

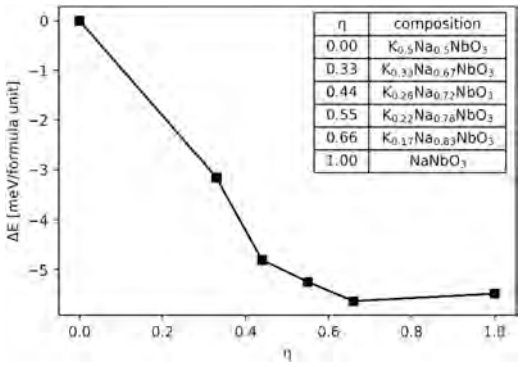

Fig. 13. *ΔE(η) renormalized per unit cell. The inset table shows the mapping between values of η and concentrations in $K_xNa_{1-x}NbO_3$. Exemplarily, Na-rich compositions are depicted in the inset table, but in this DFT analysis they are accompanied by mirrored K-rich compositions. This is different from the complex experimental observation that Na-rich KNN is accompanied by alkali-poor (yet K-rich) pyrochlore phase.*

realistic model DFT results at zero temperature would unlikely provide definitive conclusions. A proper treatment would necessarily involve thermodynamic aspects, such as mixing entropies and chemical potentials, which however exceed the scope of the present work. What we ultimately stress is, however, that already at the T = 0 K level a tendency to a partial segregation into Na-rich and K-rich phases is revealed.

4. Discussion

Throughout this work, it has been shown that RF-deposited KNN films display characteristics that depend on deposition pressure (Ar flow) and post-processing conditions (annealing temperature). As deposited, KNN films are amorphous and develop crystalline features only upon annealing at 500, 600, or 700 °C. Despite achieving the required perovskite ABO_3 phase with controlled (001)/(100) orientation and large out-of-plane *c*-parameter, several measurements evidenced various levels of crystallinity, ferroelectricity, segregation, and contamination with spurious phases. Deposition of KNN in low and medium-pressure regimes promotes higher crystallinity, more (001) orientation, and correspondingly higher switching currents. This phenomenon can be attributed to the higher energy and enhanced diffusivity of Ar ions at lower pressures. Annealing at high temperatures can further enhance the crystallinity and ferroelectricity of the perovskite phase. Yet, this is accompanied by diffusion and unequal evaporation of alkali elements. In turn, segregation into two very different compositions occurs, giving rise to a stable Na-rich KNN perovskite phase and an unstable alkali deficient pyrochlore phase.

The segregation of polar and non-polar phases in KNN films has not been widely addressed in literature. In some reports, segregation has been observed to depend on process parameters such as, growth temperature, plasma composition and annealing atmosphere [18,51]. For example, Mahesh and Pamu [32] observed secondary peaks of $K_2Nb_6O_{16}$ in XRD θ-2θ spectra in KNN films grown at 400 °C by sputtering at reduced amount of oxygen. Tian et al. found $K_2Nb_8O_{21}$ and $K_4Nb_6O_{17}$ pyrochlore phases in PLD-grown KNN films, which do not appear at high deposition temperatures (> 680 °C). Also, Anh et al. found $K_4Nb_6O_{17}$ spurious phases in alkali deficient KNN films ((Na+K)/Nb = 0.85) deposited by chemical solution deposition from precursor solutions with stoichiometric amounts of Na and K [52]. When films are produced with alkali excess, higher perovskite fractions are obtained [49,53].

Regarding morphological and crystallization features, in chemically deposited KNN films, Jacques et al. [19,54] observed "rosettes", i.e. circular-shaped perovskite disks around nucleation centers, growing in area and numbers with increasing annealing time within a pyrochlore amorphous matrix. Similar to our case, they found that Nb remains uniformly distributed in the film, while K and Na segregate. Although they did not pursue estimation of stoichiometry, the rosettes were measured to be Na rich, like the volcano features we observed in our KNN films. They hypothesized that the composition of the perovskite phase, unbalanced towards Na, could be due to a higher diffusion coefficient for Na through Nb_2O_5, with respect to K. Other than our report and those of Jacques et al., the nucleation and growth of featured perovskites phases has only been studied for PZT films [55,56]. For instance, Kwok and Desu have observed that circular shapes, identified as the perovskite phase, nucleate in a pyrochlore matrix. The nucleation sites increase in number as a function of annealing time and temperature above 525 °C, underlining the strong dependence of perovskite formation with temperature [15,33]. The formation of rosettes has been explained using the Johnson-Mehl-Avrami-Kolmogorov (JMAK) model, that describes, in general, phase transition kinetics and can also be applied to thin films. The mechanisms are well explained in the work of Tomellini and Fanfoni [57,58]. According to this model, phase transformation occurs by nucleation, and the nucleation sites are distributed in the volume in a random fashion. Therefore, the centers of the rosettes are the nucleation points, and the circles surrounding them, the grown phase.

From the cited KNN and PZT studies, we can suggest that when KNN films are deposited amorphous, at a relatively low temperature of 500 °C, and in oxygen-deficient atmosphere, annealing in a partial oxygen atmosphere initiates crystallization of the film into the desirable KNN perovskite phase. However, due to evident alkali deficiency and insufficient temperature, only certain regions can reach the correct stoichiometry to form the ABO_3 perovskite composition [49]. The characteristic volcano features are due to the appearance of nucleation centers initiated by oxygen and alkali diffusion. These regions, however, do not exhibit the 50/50 Na/K ratio of the KNN parent target but rather a 70/30 composition, which appears to be thermodynamically favored as Na migrates within the film. This consequently produces significant alkali deficiency in other regions, and secondary phases that easily degrade in wet environments. The formation of Na-rich and K-rich perovskite phases starting from a stoichiometric $K_{0.5}Na_{0.5}NbO_3$ system was also suggested by our initial DFT studies, which showed a tendency for partial segregation at T = 0 K. Future studies will also include thermodynamic considerations to study the most stable compositions.

Even though we have already mentioned the importance of oxygen, its role in segregation and perovskite formation must be further emphasized and studied. Preliminary studies of us indicate that if oxygen is removed from the annealing atmosphere, the films remain very uniform and homogeneous, both compositionally and morphologically. Nonetheless, they do not achieve crystallization and do not exhibit ferroelectric response. Segregation happens because, for an oxygen-deficient film, addition of oxygen at high temperature ignites the seeding of a sodium rich perovskite phase, which is the preferred thermodynamic phase in these conditions. By adding oxygen during the KNN sputtering stage, we have recently observed that segregation can be partially reduced in $K_{0.5}Na_{0.5}NbO_3$ films. We argue that potential improvements for large-scale fabrication of KNN films will come from fine tuning of oxygen in the plasma atmosphere, adoption of Na-rich compositions, increase in alkali ion content in the parent KNN target, better control of annealing conditions, and doping for enhanced stability and performance.

5. Conclusions

Initially amorphous $K_{0.5}Na_{0.5}NbO_3$ films were deposited at 500 °C on $Pt(111)/TiO_2/SiO_2/Si$ wafers by RF sputtering. Post-annealed samples showed varying degrees of ferroelectricity due to crystallization of the films in (001)/(100) mixed-orientation. Annealing, however, also caused varying degrees of segregation of phases. The strongest ferroelectric responses were obtained in significantly segregated KNN films fabricated in highly energetic conditions (low Ar pressure and high

annealing temperature). Compositional analysis performed by EDX, coupled with C-AFM electrical imaging and local measurements, evidenced two very distinct regions. Crystalline, stable Na-rich islands resembling volcanoes with perovskite compositions ranging from $K_{0.3}Na_{0.7}NbO_3$ to $K_{0.21}Na_{0.79}NbO_3$ were found to be the origin of the macro ferroelectricity ($2Pr = 21\ \mu C/cm^2$); these compositions are near to the other two morphotropic phase boundaries of KNN. On the contrary, surrounding areas correspond better with a K-rich $A_4Nb_6O_{17}$ alkali-deficient pyrochlore phase that is non-ferroelectric, morphologically rough, electrically leaky, and chemically unstable. A favorable Na accumulation into circular spots occurs spontaneously during annealing in partial O2 atmosphere, while K is lost extensively. This suggests that Na-rich perovskite phases are inherently more stable for KNN film systems grown at relatively low temperature under high plasma energy conditions. Initial DFT assessment also supports that segregation in KNN might be favored towards Na-rich and K-rich combinations. Further studies will be directed at understanding the ferroelectric performance, chemical uniformity, and thermodynamic stability of several Na-rich-$K_xNa_{1-x}NbO_3$ solid solutions deposited by large-scale co-sputtering.

CRediT authorship contribution statement

Pavese Giulia: Writing – review & editing, Writing – original draft, Investigation, Formal analysis, Data curation, Conceptualization. **Orlando Federico:** Writing – original draft, Methodology, Formal analysis, Data curation. **Picozzi Silvia:** Writing – original draft, Validation, Methodology, Conceptualization. **Albisetti Edoardo:** Validation, Formal analysis. **Castoldi Laura:** Validation, Resources, Project administration, Funding acquisition, Conceptualization. **Bertacco Riccardo:** Writing – review & editing, Writing – original draft, Resources, Project administration, Investigation, Funding acquisition, Data curation, Conceptualization. **Badillo-Avila Miguel Angel:** Writing – review & editing, Writing – original draft, Validation, Supervision, Methodology, Investigation, Formal analysis, Data curation, Conceptualization. **Asa Marco:** Supervision, Resources, Methodology, Conceptualization. **Melzi Fabio:** Writing – review & editing, Validation, Resources. **Maspero Federico:** Writing – original draft, Supervision, Investigation, Formal analysis.

Declaration of Competing Interest

The authors declare the following financial interests/personal relationships which may be considered as potential competing interests: Riccardo Bertacco reports financial support was provided by STMicroelectronics. Fabio Melzi reports a relationship with STMicroelectronics that includes: employment. Laura Castoldi reports a relationship with STMicroelectronics that includes: employment. If there are other authors, they declare that they have no known competing financial interests or personal relationships that could have appeared to influence the work reported in this paper.

Acknowledgments

This work was supported by the Joint Research Centre STEAM between Politecnico di Milano and STMicroelectronics. The authors acknowledge the availability of experimental facilities at PoliFAB. We would like to express our gratitude to Valerio Levati for his help with AFM and C-AFM measurements and data collection.

Appendix A. Supporting information

Supplementary data associated with this article can be found in the online version at doi:10.1016/j.jallcom.2025.180039.

References

[1] M.-G. Kang, W.-S. Jung, C.-Y. Kang, S.-J. Yoon, Recent progress on PZT based piezoelectric energy harvesting technologies, Actuators 5 (2016) 5, https://doi.org/10.3390/act5010005.
[2] A. Aabid, M.A. Raheman, Y.E. Ibrahim, A. Anjum, M. Hrairi, B. Parveez, N. Parveen, J. Mohammed Zayan, A systematic review of piezoelectric materials and energy harvesters for industrial applications, Sensors 21 (2021) 4145, https://doi.org/10.3390/s21124145.
[3] J. Rodel, W. Jo, K. Seifert, E.-M. Anton, T. Granzow, D. Damjanovic, Perspective on the development of lead-free piezoceramics, J. Am. Ceram. Soc. 92 (2009), https://doi.org/10.1111/j.1551-2916.2009.03061.x.
[4] Y. Saito, H. Takao, T. Tani, T. Nonoyama, K. Takatori, T. Homma, T. Nagaya, M. Nakamura, Lead-free piezoceramics, Nature 432 (2004) 84–87, https://doi.org/10.1038/nature03028.
[5] K. Xu, J. Li, X. Lv, J. Wu, X. Zhang, D. Xiao, J. Zhu, Superior piezoelectric properties in potassium–sodium niobate lead-free ceramics, Adv. Mater. 28 (2016) 8519–8523, https://doi.org/10.1002/adma.201601859.
[6] V.M. Kugler, F. Söderlind, D. Music, U. Helmersson, J. Andreasson, T. Lindbäck, Low temperature growth and characterization of (Na,K)NbO_x thin films, J. Cryst. Growth 254 (2003) 400–404, https://doi.org/10.1016/S0022-0248(03)01184-9.
[7] H.J. Seog, A. Ullah, C.W. Ahn, I.W. Kim, S.Y. Lee, J. Park, H.J. Lee, S.S. Won, S.-H. Kim, Recent Progress in Potassium sodium niobate lead-free thin films, J. Korean Phys. Soc. 72 (2018) 1467–1483, https://doi.org/10.3938/jkps.72.1467.
[8] C. Groppi, F. Maspero, A. Rovelli, M. Asa, G. Malavena, C.M. Compagnoni, E. Albisetti, S. Vangelista, M.A. Badillo-Ávila, R. Bertacco, Electrode-dependent asymmetric conduction mechanisms in $K_{0.5}Na_{0.5}NbO_3$ micro-capacitors, Mater. Sci. Semicond. Process 160 (2023) 107422, https://doi.org/10.1016/j.mssp.2023.107422.
[9] C. Groppi, F. Maspero, M. Asa, G. Pavese, C. Rinaldi, E. Albisetti, M. Badillo-Avila, R. Bertacco, Spontaneous pattern of orthogonal ferroelectric domains in epitaxial KNN films, J. Appl. Phys. 134 (2023) 204102, https://doi.org/10.1063/5.0171349.
[10] C.W. Ahn, S.Y. Lee, H.J. Lee, A. Ullah, J.S. Bae, E.D. Jeong, J.S. Choi, B.H. Park, I. W. Kim, The effect of K and Na excess on the ferroelectric and piezoelectric properties of $K_{0.5}Na_{0.5}NbO_3$ thin films, J. Phys. Appl. Phys. 42 (2009) 215304, https://doi.org/10.1088/0022-3727/42/21/215304.
[11] H.-S. Ma, M.-K. Lee, B.-H. Kim, K.-H. Park, J.-J. Park, S.-H. Lee, Y.-G. Jeong, K.-I. Park, C.K. Jeong, G.-J. Lee, Role of oxygen vacancy defects in piezoelectric thermal stability characteristics of Mn-doped (K,Na,Li)NbO_3 piezoceramics, Ceram. Int. 47 (2021) 27803–27815, https://doi.org/10.1016/j.ceramint.2021.06.207.
[12] I.P. Lipscomb, P.M. Weaver, J. Swingler, J.W. McBride, The effect of relative humidity, temperature and electrical field on leakage currents in piezo-ceramic actuators under dc bias, Sens. Actuators Phys. 151 (2009) 179–186, https://doi.org/10.1016/j.sna.2009.01.017.
[13] L. Song, S. Glinsek, E. Defay, Toward low-temperature processing of lead zirconate titanate thin films: advances, strategies, and applications, Appl. Phys. Rev. 8 (2021) 041315, https://doi.org/10.1063/5.0054004.
[14] S. Kukushkin, I. Tentilova, P. Igor, Mechanism of the phase transformation of the pyrochlore phase into the perovskite phase in lead zirconate titanate films on silicon substrates, Phys. Solid State 54 (2012), https://doi.org/10.1134/S1063783412030158.
[15] C.K. Kwok, S.B. Desu, Formation kinetics of $PbZr_xTi_{1-x}O_3$ thin films, J. Mater. Res. 9 (1994) 1728–1733, https://doi.org/10.1557/JMR.1994.1728.
[16] C.K. Kwok, S.B. Desu, Pyrochlore to perovskite phase transformation in sol-gel derived lead-zirconate-titanate thin films, Appl. Phys. Lett. 60 (1992) 1430–1432, https://doi.org/10.1063/1.107312.
[17] V.S. Tiwari, A. Kumar, V.K. Wadhawan, D. Pandey, Kinetics of formation of the pyrochlore and perovskite phases in sol-gel derived lead zirconate titanate powder, J. Mater. Res. 13 (1998) 2170–2173, https://doi.org/10.1557/JMR.1998.0303.
[18] B.-Y. Kim, T.-G. Seong, I.-T. Seo, M.-S. Jang, S. Nahm, J.-Y. Kang, S.-J. Yoon, Effects of annealing atmosphere on the structural and electrical properties of ($Na_{0.5}K_{0.5}$)NbO_3 Thin films grown by RF magnetron sputtering, Acta Mater. 60 (2012) 3107–3112, https://doi.org/10.1016/j.actamat.2012.02.015.
[19] L. Jacques, V. Kovacova, J.I. Yang, S. Trolier-McKinstry, Activation energies for crystallization of manganese-doped (K,Na)NbO_3 thin films deposited from a chemical solution, J. Am. Ceram. Soc. 104 (2021) 4968–4976, https://doi.org/10.1111/jace.17915.
[20] S. Sharma, A. Kumar, V. Gupta, M. Tomar, Dielectric and ferroelectric studies of KNN thin film grown by pulsed laser deposition technique, Vacuum 160 (2019) 233–237, https://doi.org/10.1016/j.vacuum.2018.11.036.
[21] H.E. Mgbemere, R.-P. Herber, G.A. Schneider, Investigation of the dielectric and piezoelectric properties of potassium sodium niobate ceramics close to the phase boundary at ($K_{0.35}Na_{0.65}$)NbO_3 and partial substitutions with lithium and antimony, J. Eur. Ceram. Soc. 29 (2009) 3273–3278, https://doi.org/10.1016/j.jeurceramsoc.2009.05.021.
[22] Pamu, Structural, mechanical and optical properties of nanocrystalline ($K_{0.34}Na_{0.65}$)$NbO_{3.01}$ thin films deposited by RF sputtering, J. Ceram. Sci. Tech. (2014), https://doi.org/10.4416/JCST2013-00026.
[23] G. Kresse, J. Furthmüller, Efficient iterative schemes for ab initio total-energy calculations using a plane-wave basis set, Phys. Rev. B 54 (1996) 11169–11186, https://doi.org/10.1103/PhysRevB.54.11169.
[24] J.P. Perdew, A. Ruzsinszky, G.I. Csonka, O.A. Vydrov, G.E. Scuseria, L. A. Constantin, X. Zhou, K. Burke, Restoring the density-gradient expansion for exchange in solids and surfaces, Phys. Rev. Lett. 100 (2008) 136406, https://doi.org/10.1103/PhysRevLett.100.136406.

[25] P.E. Blöchl, Projector augmented-wave method, Phys. Rev. B 50 (1994) 17953–17979, https://doi.org/10.1103/PhysRevB.50.17953.
[26] A. Zunger, S.-H. Wei, L.G. Ferreira, J.E. Bernard, Special quasirandom structures, Phys. Rev. Lett. 65 (1990) 353–356, https://doi.org/10.1103/PhysRevLett.65.353.
[27] M. Ångqvist, W.A. Muñoz, J.M. Rahm, E. Fransson, C. Durniak, P. Rozyczko, T. H. Rod, P. Erhart, ICET – A python library for constructing and sampling alloy cluster expansions, Adv. Theory Simul. 2 (2019) 1900015, https://doi.org/10.1002/adts.201900015.
[28] T.S.T. Schimizu, T.K.T. Kawakubo, First-principles approach to the effect of c-axis elongation of $BaTiO_3$ thin films, Jpn. J. Appl. Phys. 37 (1998) L235, https://doi.org/10.1143/JJAP.37.L235.
[29] Plasma Dynamics, in: Princ. Plasma Disch. Mater. Process, John Wiley & Sons, Ltd, 2005, pp. 87–132, 10.1002/0471724254.ch4.
[30] J. Tellier, B. Malic, B. Dkhil, D. Jenko, J. Cilensek, M. Kosec, Crystal structure and phase transitions of sodium potassium niobate perovskites, Solid State Sci. 11 (2009) 320–324, https://doi.org/10.1016/j.solidstatesciences.2008.07.011.
[31] H. Bruncková, Ľ. Medvecký, P. Hvizdoš, Effect of substrate on microstructure and mechanical properties of sol–gel prepared (K,Na)NbO_3 thin films, Mater. Sci. Eng. B 178 (2013) 254–262, https://doi.org/10.1016/j.mseb.2012.12.003.
[32] P. Mahesh, D. Pamu, Effect of deposition temperature on structural, mechanical, optical and dielectric properties of radio frequency sputtered nanocrystalline (K_xNa_{1-x})NbO_3 thin films, Thin Solid Films 562 (2014) 471–477, https://doi.org/10.1016/j.tsf.2014.04.007.
[33] C.K. Kwok, S.B. Desu, Low temperature perovskite formation of lead zirconate titanate thin films by a seeding process, J. Mater. Res. 8 (1993) 339–344, https://doi.org/10.1557/JMR.1993.0339.
[34] G.L. Brennecka, C.M. Parish, B.A. Tuttle, L.N. Brewer, M.A. Rodriguez, Reversibility of the perovskite-to-fluorite phase transformation in lead-based thin and ultrathin films, Adv. Mater. 20 (2008) 1407–1411, https://doi.org/10.1002/adma.200702442.
[35] C.-S. Park, J.-W. Lee, S.-M. Lee, S.-H. Jun, H.-E. Kim, Effect of excess PbO on microstructure and orientation of PZT(60/40) films, J. Electroceram. 25 (2010) 20–25, https://doi.org/10.1007/s10832-009-9584-9.
[36] T. Schenk, E. Yurchuk, S. Mueller, U. Schroeder, S. Starschich, U. Böttger, T. Mikolajick, About the deformation of ferroelectric hystereses, Appl. Phys. Rev. 1 (2014) 041103, https://doi.org/10.1063/1.4902396.
[37] S. Sharma, A. Kumar, V. Gupta, M. Tomar, Dielectric and ferroelectric studies of KNN thin film grown by pulsed laser deposition technique, Vacuum 160 (2019) 233–237, https://doi.org/10.1016/j.vacuum.2018.11.036.
[38] J.S. Kim, H.J. Lee, S.Y. Lee, I.W. Kim, S.D. Lee, Frequency and temperature dependence of dielectric and electrical properties of radio-frequency sputtered lead-free $K_{0.48}Na_{0.52}NbO_3$ thin films, Thin Solid Films 518 (2010) 6390–6393, https://doi.org/10.1016/j.tsf.2010.02.078.
[39] K. Shibata, K. Watanabe, T. Kuroda, T. Osada, KNN lead-free piezoelectric films grown by sputtering, Appl. Phys. Lett. 121 (2022) 092901, https://doi.org/10.1063/5.0104583.
[40] A. Marthinsen, C. Faber, U. Aschauer, N.A. Spaldin, S.M. Selbach, Coupling and competition between ferroelectricity, magnetism, strain, and oxygen vacancies in $AMnO_3$ perovskites, MRS Commun. 6 (2016) 182–191, https://doi.org/10.1557/mrc.2016.30.
[41] H.J. Lee, I.W. Kim, J.S. Kim, C.W. Ahn, B.H. Park, Ferroelectric and piezoelectric properties of $Na_{0.52}K_{0.48}NbO_3$ thin films prepared by radio frequency magnetron sputtering, Appl. Phys. Lett. 94 (2009) 092902, https://doi.org/10.1063/1.3095500.
[42] I. Kanno, T. Mino, S. Kuwajima, T. Suzuki, H. Kotera, K. Wasa, Piezoelectric properties of (K,Na)NbO_3 thin films deposited on (001)$SrRuO_3$/Pt/MgO substrates, 2562–2556, IEEE Trans. Ultrason. Ferroelectr. Freq. Control 54 (2007), https://doi.org/10.1109/TUFFC.2007.577.
[43] J. Huang, J. Liu, Z. Li, K. Zhu, B. Wang, Q. Gu, B. Feng, J. Qiu, Effects of annealing temperature on structure and electrical properties of (Na,K)NbO_3 thin films grown by RF magnetron sputtering deposition, J. Mater. Sci. Mater. Electron 27 (2016) 899–905, https://doi.org/10.1007/s10854-015-3832-3.
[44] L.-Q. Cheng, K. Wang, F.-Z. Yao, F. Zhu, J.-F. Li, Composition inhomogeneity due to alkaline volatilization in Li-modified (K,Na)NbO_3 lead-free piezoceramics, J. Am. Ceram. Soc. 96 (2013) 2693–2695, https://doi.org/10.1111/jace.12497.
[45] X. Wang, S. Olafsson, L.D. Madsen, S. Rudner, I.P. Ivanov, A. Grishin, U. Helmersson, Growth and characterization of $Na_{0.5}K_{0.5}NbO_3$ thin films on polycrystalline $Pt_{80}Ir_{20}$ substrates, J. Mater. Res. 17 (2002) 1183–1191, https://doi.org/10.1557/JMR.2002.0175.
[46] A. Herrmann, E. Schumacher, L. Wöste, Preparation and photoionization potentials of molecules of sodium, potassium, and mixed atoms, J. Chem. Phys. 68 (1978) 2327–2336, https://doi.org/10.1063/1.436003.
[47] X. Wang, Y. Huan, Z. Wang, X. Lin, S. Huang, T. Wei, L. Li, X. Wang, Electrical conduction and dielectric relaxation mechanisms in the KNN-based ceramics, J. Appl. Phys. 126 (2019) 104101, https://doi.org/10.1063/1.5110582.
[48] B. Malic, D. Jenko, J. Holc, M. Hrovat, M. Kosec, Synthesis of sodium potassium niobate: a diffusion couples study, J. Am. Ceram. Soc. 91 (2008) 1916–1922, https://doi.org/10.1111/j.1551-2916.2008.02376.x.
[49] N. Helth Gaukås, S.M. Dale, T.M. Ræder, A. Toresen, R. Holmestad, J. Glaum, M.-A. Einarsrud, T. Grande, Controlling phase purity and texture of $K_{0.5}Na_{0.5}NbO_3$ thin films by aqueous chemical solution deposition, Materials 12 (2019) 2042, https://doi.org/10.3390/ma12132042.
[50] C.L. Yaws, Handbook of Vapor Pressure Inorganic Compounds and Elements, Gulf Professional Publishing, 1995, 410.1016/s1874-8813(06)x8001-0.
[51] P. Pop-Ghe, N. Wolff, A. Rubab, L. Kienle, E. Quandt, Tailoring growth modes by excess alkali addition in magnetron sputtered potassium sodium niobate thin films, Mater. Today Commun. 27 (2021) 102221, https://doi.org/10.1016/j.mtcomm.2021.102221.
[52] C.W. Ahn, H.-I. Hwang, K.S. Lee, B.M. Jin, S. Park, G. Park, D. Yoon, H. Cheong, H. J. Lee, I.W. Kim, Raman spectra study of $K_{0.5}Na_{0.5}NbO_3$ ferroelectric thin films, Jpn. J. Appl. Phys. 49 (2010) 095801, https://doi.org/10.1143/JJAP.49.095801.
[53] K. Tanaka, H. Hayashi, K. Kakimoto, H. Ohsato, T. Iijima, Effect of (Na,K)-excess precursor solutions on alkoxy-derived (Na,K)NbO_3 powders and thin films, Jpn. J. Appl. Phys. 46 (2007) 6964, https://doi.org/10.1143/JJAP.46.6964.
[54] L. Jacques, Thesis, Chemical solution deposition of potassium sodium niobate thin films, Pa. State Univ. (2021).
[55] Z.J. Wang, Y. Aoki, L.J. Yan, H. Kokawa, R. Maeda, Crystal structure and microstructure of lead zirconate titanate (PZT) thin films with various Zr/Ti ratios grown by hybrid processing, J. Cryst. Growth 267 (2004) 92–99, https://doi.org/10.1016/j.jcrysgro.2004.03.011.
[56] A.H. Carim, B.A. Tuttle, D.H. Doughty, S.L. Martinez, Microstructure of solution-processed lead zirconate titanate (PZT) thin films, J. Am. Ceram. Soc. 74 (1991) 1455–1458, https://doi.org/10.1111/j.1151-2916.1991.tb04130.x.
[57] M. Tomellini, M. Fanfoni, Connection between phantom and spatial correlation in the Kolmogorov–johnson–mehl–Avrami-model: a brief review, Phys. Stat. Mech. Appl. 590 (2022) 126748, https://doi.org/10.1016/j.physa.2021.126748.
[58] M. Fanfoni, M. Tomellini, The Johnson-mehl- Avrami-kohnogorov model: a brief review, Il Nuovo Cim. D. 20 (1998) 1171–1182, https://doi.org/10.1007/BF03185527.